

Comparison between pulsed laser and frequency-domain photoacoustic modalities: Signal-to-noise ratio, contrast, resolution, and maximum depth detectivity

Bahman Lashkari^{a)} and Andreas Mandelis^{b)}

Center for Advanced Diffusion-Wave Technologies (CADIFT), Department of Mechanical and Industrial Engineering, University of Toronto, Toronto, M5S 3G8, Canada

(Received 9 March 2011; accepted 12 August 2011; published online 15 September 2011)

In this work, a detailed theoretical and experimental comparison between various key parameters of the pulsed and frequency-domain (FD) photoacoustic (PA) imaging modalities is developed. The signal-to-noise ratios (SNRs) of these methods are theoretically calculated in terms of transducer bandwidth, PA signal generation physics, and laser pulse or chirp parameters. Large differences between maximum (peak) SNRs were predicted. However, it is shown that in practice the SNR differences are much smaller. Typical experimental SNRs were 23.2 dB and 26.1 dB for FD-PA and time-domain (TD)-PA peak responses, respectively, from a subsurface black absorber. The SNR of the pulsed PA can be significantly improved with proper high-pass filtering of the signal, which minimizes but does not eliminate baseline oscillations. On the other hand, the SNR of the FD method can be enhanced substantially by increasing laser power and decreasing chirp duration (exposure) correspondingly, so as to remain within the maximum permissible exposure guidelines. The SNR crossover chirp duration is calculated as a function of transducer bandwidth and the conditions yielding higher SNR for the FD mode are established. Furthermore, it was demonstrated that the FD axial resolution is affected by both signal amplitude and limited chirp bandwidth. The axial resolution of the pulse is, in principle, superior due to its larger bandwidth; however, the bipolar shape of the signal is a drawback in this regard. Along with the absence of baseline oscillation in cross-correlation FD-PA, the FD phase signal can be combined with the amplitude signal to yield better axial resolution than pulsed PA, and without artifacts. The contrast of both methods is compared both in depth-wise (delay-time) and fixed delay time images. It was shown that the FD method possesses higher contrast, even after contrast enhancement of the pulsed response through filtering. © 2011 American Institute of Physics. [doi:10.1063/1.3632117]

I. INTRODUCTION

In the past decade, the field of biomedical photoacoustics (PA) has expanded vastly. Imaging and tomography have always been a major part of this research area and are discussed in recent review papers.^{1,2} A hybrid technique, the PA method combines the benefits of both ultrasound and optical methods. Another attractive feature of PA is its intrinsic potential for combination with ultrasound in a dual-mode instrument (“co-registration”). These features can improve sensitivity and increase the chances of early cancer detection.

It has been more than a decade since the first PA breast cancer imaging instrument was reported.^{3,4} Also within a few years, another system with the same intent was developed.⁵ These instruments have also been clinically assessed in comparison with ultrasound and x-ray mammography.^{6,7} The prevailing excitation technique has always been the use of nanosecond laser pulses, not only in PA breast cancer diagnosis but also in other PA imaging applications. These short pulses generate powerful acoustic transients which facilitate signal detection. Moreover, the depth of the acoustic source or the chromophore can readily be determined. The

alternative approach, utilizing a long duration, low power intensity modulated laser source has also been introduced.^{8–10}

The major motivation for the latter method, called continuous wave (CW) or frequency-domain (FD)-PA, is the availability of compact and inexpensive CW laser diodes with a wide wavelength selection in comparison with bulky and expensive Q-switched pulsed lasers, thereby raising the possibility for portable, sensitive PA imagers. The FD modality is capable of generating a high peak power cross-correlation response through matched filtering.¹¹ Another favorable aspect of the FD method is its depth-selective imaging capacity.^{10,12}

Along with developing PA systems with promising clinical applications, the limits of PA for medical imaging have been under investigation. The most important characteristics affecting the functionality of the method are maximum sensitivity, resolution, and contrast: how deeply it is capable of detecting the tumorous lesions, and how small and different from healthy tissue might these lesions be. The main limitations of all optical methods are the large attenuation of light in the tissue and large baselines which compromise dynamic range, preventing these methods from detecting deep-seated tumors. The maximum detectivity also depends on the absorption coefficient (the blood content) of the tumor. Considering these issues along with other limiting factors such as transducer thermal noise and sensitivity, Oraevsky and

^{a)}Electronic mail: bahman@mie.utoronto.ca.

^{b)}Author to whom correspondence should be addressed. Electronic mail: mandelis@mie.utoronto.ca. Tel.: 416-978-1287. Fax: 416-978-6160.

Karabutov presented a prediction for the ultimate sensitivity of their system.¹³ They determined the proper bandwidth for detection of the transient and estimated that the PA system is capable of detecting a 1 mm tumor in the depth of 7 cm in human tissue. Nevertheless, clinical trials report the detection of tumors no deeper than ~ 2 cm.⁶ Another related study on the maximum detectivity of PA was performed by Ku and Wang.¹⁴ Using optical contrast agents, they demonstrated the capability of PA to detect a blood vessel with enhanced absorption as small as 0.3 mm in diameter beneath 5 cm of chicken breast.

The sensitivity of the PA method has mostly been discussed in relation to the pulsed excitation method, but the advent of the alternative FD-PA modality^{8–10} compelled a comparison between the signal-to-noise ratio (SNR) of both techniques.¹⁵ Maslow and Wang used the maximum permissible exposure (MPE) difference between the two methods and calculated six orders of magnitude of difference between the corresponding acoustic transients. Taking into account the effect of the transducer bandwidth and sensitivity, they estimated the SNR of FD-PA to be 20–40 dB less than the pulsed method. However, with what is known about other imaging methods which utilize both time-domain (TD) and FD methods, this conclusion is unexpected. For instance, FD optical coherence tomography (OCT) utilizing a swept laser source was predicted to produce 20–30 dB higher SNR over TD-OCT.¹⁶ Clinical comparative studies also support the reliability and higher resolution of FD-OCT.¹⁷ A more relevant case is the comparison of the FD and TD techniques in pure ultrasound imaging, where it has been predicted that the FD method is capable of attaining 15–20 dB higher SNR than the pulsed method.¹⁸ Superiority of the FD mode ultrasound is also demonstrated in clinical experiments; CW ultrasound could significantly increase the imaging depth, almost by 2 cm.¹⁹ Furthermore, a comparative study on the maximum detectivity of FD and TD PA methods conducted by Telenkov and Mandelis²⁰ showed that at low frequency (500 kHz), the maximum detectable depth by the two methods is comparable, while at higher frequency (3.5 MHz), the pulsed method provides deeper detectivity. Recent estimates by these authors also predict SNR of 25 dB and 8 dB for TD and FD PA, respectively, for an absorber ($\mu_a = 2 \text{ cm}^{-1}$) inside 3 cm of the tissue.²¹ This estimate ignores the acoustic attenuation as well as transducer band-pass effects. Very recently, Petschke and La Rivière²² presented a theoretical comparison between TD and FD PA modalities and concluded that the SNR of FD-PA is 20–30 dB worse than that of TD-PA and both methods generate same axial-resolution. These results are achieved by assuming a rectangular transducer spectrum and identical bandwidth for both methods.

This short review raises the necessity for additional investigations, both experimental and theoretical, to resolve the ambiguities that exist in relation to FD and TD PA. Here, we do not intend to present a pure and abstract comparison between the two modalities, but rather we focus on the options each modality provides and use this opportunity to examine the possibility of manipulating different parameters to maximize the performance of the imaging system. The working options in the application of the pulsed method are mainly re-

stricted to the laser wavelength and power, transducer choices, the pulse repetition frequency (PRF), and signal apodization. Most of these items are predefined in the system. However, working with a FD-PA system in addition to those options, one can change many parameters, such as chirp waveform, duration, and bandwidth. The present PA application is breast cancer diagnosis simulation, leading to imaging optimization through manipulation of the aforementioned parameters. It is emphasized that the comparison strategy adopted in this work is to characterize PA imaging by exploiting the capabilities and advantages of both modalities under identical sample configuration conditions and within the limitations (energy/power ceiling) imposed by the MPE curve. Each method stands with its own features against a given imaging or absorber detection task.

II. EXPERIMENTAL SET-UP AND SIGNAL PROCESSING

Experiments were performed with a dual-mode PA system²⁰ which provides the possibility of comparative study between the pulsed and CW modalities. The implementation of the dual-mode PA imaging system is shown in Fig. 1. By sliding one mirror, we can switch between the CW and pulsed lasers. Both laser beams impinged on the same spot, and the positions of the ultrasonic transducer and sample were fixed. The wavelength of both lasers was 1064 nm. The pulsed source was a Q-switched Nd:YAG laser (Continuum, Santa-Clara, CA) which produces pulses of 5.2 ns duration. The PRF was fixed at 10 Hz. The CW source features a fiber laser (IPG Photonics, Boston, MA) and an acousto-optic modulator (AOM) which modulates the laser intensity according to waveforms defined in the software function generator. The pulsed and CW laser beam diameters were 4 mm and 2.8 mm, respectively.

Two single focused ultrasonic transducers were used with central frequencies 0.5 MHz and 3.5 MHz and focal lengths 5.27 cm and 2.54 cm, respectively. To transmit the PA signals to the software, analog-to-digital (ADC, NI PXI-5105) and NI-SCOPE software (National Instruments, Austin, TX) were used. In the FD mode, to feed the waveform to the AOM, digital-to-analog converter (DAC, NI PXIe-5442) and NI-FGEN software (National Instruments, Austin, TX) were

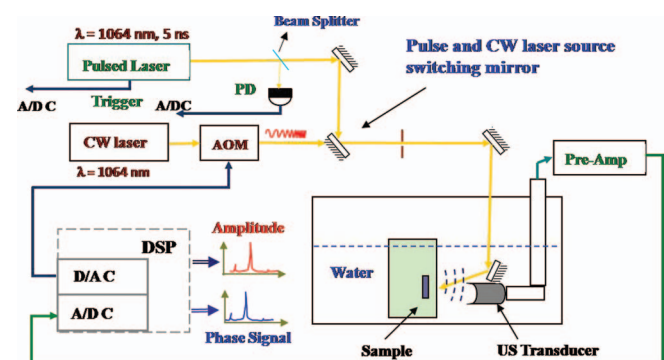


FIG. 1. (Color online) Block diagram of the pulsed and FD PA imaging and signal acquisition system.

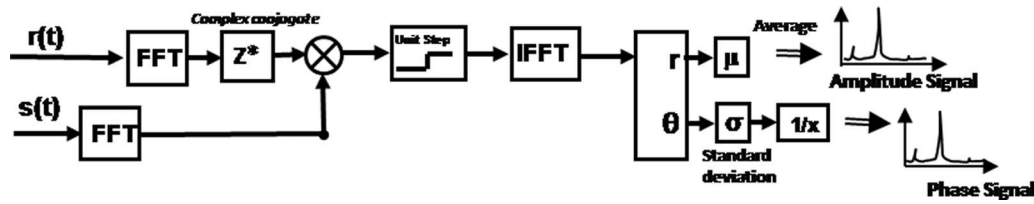


FIG. 2. Schematic signal processing flowchart for FD-PA.

utilized. An external trigger channel was employed to synchronize the detected signal with the transmitted waveform in the FD case or with the pulse discharge in the TD mode. The maximum sampling frequency of the utilized ADC was 60 MHz and that of the DAC was 100 MHz; however, during the experiments both were set to 60 MHz.

In the pulsed mode, an A-scan can be easily constructed using the time-of-flight of the acoustic transient. In the FD mode, to determine the depths of chromophores, the cross-correlation of the detected acoustic signal, $s(t)$, and the incident laser waveform, $r(t)$, was calculated. The delay time of the peak represents the subsurface position of a chromophore. The signal processing pathway (flowchart) is shown in Fig. 2. In addition to the in-phase cross-correlation, the cross-correlation of the detected signal with the quadrature of the input waveform was also calculated by eliminating the negative frequencies and making the signal analytic. The amplitude of this analytic signal provides the envelope cross-correlation. The envelope signal contains the total energy as well as the corresponding noise in the in-phase and quadrature channels. The noise level in both signals is identical, while the peak power can be higher in either of the signals. Therefore, the amplitude signal ensures a high SNR. On the other hand, the FWHM of the amplitude signal is approximately twice that of its components and, therefore, its resolution is half of the in-phase or quadrature cross-correlation.

III. TRANSIENT PRESSURE AND SNR

Theoretical simulations of laser radiation diffusion in turbid media and PA wave generation and propagation in one-dimensional (1D) as well as axisymmetric coordinates were described in Refs. 23 and 24. The solution to the diffusion limit of the Boltzmann radiative transport equation reveals that the spherical propagation and exponential attenuation approximations provide a very close estimate for laser diffusion in turbid media, particularly where the laser spotsize is very small. Employing the transfer function method, in the limit of large laser spotsize and diminishing low-frequency contributions by transducer band-pass effects, simplifies the problem and 1D PA theory can be used to predict the maximum pressure generated with both TD and FD PA excitation. The optimal chirp bandwidths with specific ultrasonic transducers generating the highest FD-PA peak have been identified²³ and are also used in the present work.

The 1D solution for a two-layer model for a laser-induced pressure transient generated at the surface of an absorber inside a turbid medium can be used to calculate the back-

propagating PA pressure detected by a transducer:²³

$$\tilde{p}_s(f) = \frac{\Gamma_a}{\left(1 + \frac{\rho_a c_a}{\rho_s c_s}\right)} \left(\frac{\mu_a}{\mu_a c_a + j\omega}\right) e^{-j(\omega/c_s)L} \tilde{I}(f), \quad (1)$$

where tilde indicates the Fourier transform operation; c_a and c_s are the speed of sound in the absorbing and scattering medium, respectively; ρ_a , and ρ_s are the density of absorbing and scattering medium, respectively; ω is the angular modulation frequency: $\omega = 2\pi f$; $I(t)$ is the laser intensity distribution reaching the absorber; Γ_a is the efficiency of thermo-acoustic excitation (Grüneisen coefficient); μ_a is the absorption coefficient in the absorbing medium (tumor); and L is the thickness of the scattering medium over the absorber.

The optical intensity reaching the absorbing medium can be estimated either as a 1D exponential attenuation, when the laser spotsize is large,

$$\tilde{I}(f) = \mathbf{F} [I_0(t)e^{-\mu_{eff}L}] = \tilde{I}_0(f)e^{-\mu_{eff}L}, \quad (2)$$

or for small laser spotsize, as spherical propagation and exponential attenuation,

$$\tilde{I}(f) \approx \frac{1}{2} W_0 \tilde{I}_0(f) \left(\frac{e^{-\mu_{eff}L}}{L}\right), \quad (3)$$

where $I_0(t)$ is the incident intensity, μ_{eff} is the effective optical attenuation coefficient, F symbolizes the Fourier transformation operation, and W_0 is the laser spotsize on the turbid medium. To simplify the theoretical treatment, we assume equal acoustic impedances for both media in Eq. (1), that is, $\rho_a c_a \approx \rho_s c_s$. This assumption has only a minor effect on the peak value of the signal. The effect of acoustic attenuation can be added to the model by replacing the real wavenumber with a complex counterpart in the scattering medium. This term plays a significant role at high frequencies, but is only of minor importance at low frequencies. Under these conditions, Eq. (1) becomes

$$\tilde{p}_s(f) = \frac{\Gamma_a e^{-\mu_{eff}L}}{2} \left(\frac{\mu_a}{\mu_a c_a + j\omega}\right) e^{-j(\omega/c_s)L} e^{-\alpha_s f L} \tilde{I}_0(f). \quad (4)$$

The acoustic attenuation in the scattering medium, α'_s , is considered to have a linear frequency dependence, ($\alpha'_s = \alpha_s f$) which is a proper approximation for the human breast tissue, where $\alpha_s = 0.75 \text{ dB/MHz cm} = 0.0863 \text{ Np/cm}$.²⁵ The spectra of $\tilde{p}_s(f)/\tilde{I}_0(f)$ (excluding the delay-time term) and acoustic attenuation are depicted in Fig. 3.

The effect of the transducer has been modeled²³ using the Krimholtz-Leedom-Matthaei (KLM) model.²⁶ The normalized transfer functions, \tilde{H}_{tr} , for both employed transducers

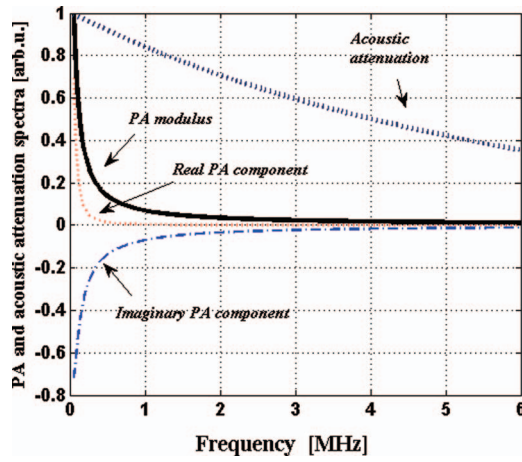


FIG. 3. (Color online) Normalized PA (excluding the delay term) and acoustic attenuation spectra. (Typical values of parameters used here: $\mu_a = 2 \text{ cm}^{-1}$, $c_s = 1.5 \text{ mm}/\mu\text{s}$, $L = 2 \text{ cm}$, $\alpha_s = 0.0863 \text{ Np/cm}$.)

are depicted in Figs. 4(a) and 4(b). The transfer functions are normalized with respect to sensitivity (η) of the transducer at peak frequency. The sensitivity of the 3.5 MHz transducer was measured at peak frequency to be $31.8 \mu\text{V}/\text{Pa}$, using a calibrated hydrophone. The frequency range of the 500 kHz transducer was outside the calibrated range of the hydrophone.

Using the PA formalism (Eq. (4)) in conjunction with the transducer transfer function model, the detected PA response voltage from the transducer can be determined:

$$V_{tr}(t) = \int_{-\infty}^{+\infty} \tilde{p}_s(f) \eta \tilde{H}_{tr}(f) e^{j\omega t} df \quad [\text{V}]. \quad (5)$$

The above formula can be used for both cases of pulsed and FD modes.

A. Pulsed PA mode

Taking the inverse Fourier transformation of Eq. (1) yields the transient pressure response to a time-dependent laser intensity $I_0(t)$, propagated back to the surface of the turbid medium,

$$p_s(t) = \frac{\Gamma_a \mu_a e^{-\mu_{eff} L}}{2} e^{-\mu_a c_a (t - (L/c_s))} H\left(t - \frac{L}{c_s}\right) * I_0(t), \quad (6)$$

where H is the Heaviside step function. Here, the asterisk denotes convolution. This equation can be used to determine the acoustic pressure transient generated by nanosecond pulsed laser irradiation:

$$I_0(t) = \frac{E_0}{\tau_0} \left[H\left(t + \frac{\tau_0}{2}\right) - H\left(t - \frac{\tau_0}{2}\right) \right], \quad (7)$$

where E_0 and τ_0 are the fluence and duration of the laser pulse, respectively. Using the convolution integral in the time-domain yields

$$p_s(t) = \frac{\Gamma_a \mu_a E_0 e^{-\mu_{eff} L}}{2\tau_0} \int_{t-\tau_0/2}^{t+\tau_0/2} e^{-\mu_a c_a (\tau - (L/c_s))} \times H\left(\tau - \frac{L}{c_s}\right) d\tau, \quad (8)$$

which can be written explicitly as

$$p_s(t) = \frac{\Gamma_a \mu_a E_0 e^{-\mu_{eff} L}}{2} \left[\frac{\sinh\left(\mu_a c_a \frac{\tau_0}{2}\right)}{\mu_a c_a \frac{\tau_0}{2}} \right] e^{-\mu_a c_a (t - (L/c_s))} \times H\left(t + \frac{\tau_0}{2} - \frac{L}{c_s}\right). \quad (9)$$

For short pulse durations, $\mu_a c_a \tau_0/2 \ll 1$, this simplifies to

$$p_s(t) = \frac{\Gamma_a \mu_a E_0 e^{-\mu_{eff} L}}{2} e^{-\mu_a c_a (t - (L/c_s))} H\left(t + \frac{\tau_0}{2} - \frac{L}{c_s}\right). \quad (10)$$

Equation (10) shows that the maximum PA pressure generated by a short pulse is

$$p_s\left(t = \frac{L}{c_s}\right) = \frac{\Gamma_a \mu_a E_0 e^{-\mu_{eff} L}}{2} \quad (11)$$

attained at $t = L/c_s$. When considering the effects of limited bandwidth detection and acoustic attenuation, it is more convenient to perform the calculations in the frequency-domain. The Fourier transform of the intensity of a rectangular laser pulse of duration τ_0 , Eq. (7), is

$$\tilde{I}_0(f) = \frac{E_0}{\tau_0} \left[\tau_0 \frac{\sin\left(f \frac{\tau_0}{2}\right)}{f \frac{\tau_0}{2}} \right] = E_0 \text{sinc}\left(f \frac{\tau_0}{2}\right). \quad (12)$$

This equation shows that the required bandwidth for a typical 10 ns pulse is 100 MHz. Ultrasonic transducers are not

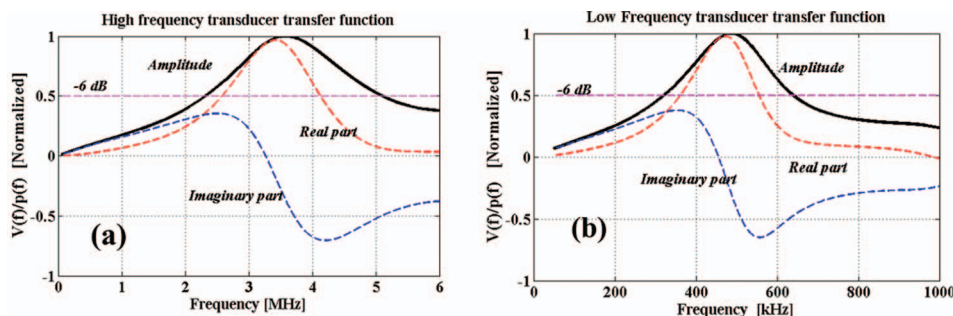


FIG. 4. (Color online) Transfer functions of (a) high-frequency (3.5 MHz) and (b) low-frequency (0.5 MHz) transducers.

usually available with such a wide bandwidth. For a fraction of 100 MHz, we can substitute $\tilde{I}_0(f) \simeq E_0$ in Eq. (4). The result is

$$\tilde{p}_s(f) = \frac{\Gamma_a E_0 e^{-\mu_{eff} L} e^{-\alpha_s f L}}{2} \left(\frac{\mu_a}{\mu_a c_a + j\omega} \right) e^{-j(\omega/c_s)L}. \quad (13)$$

To calculate the transient detected by the transducer, the KLM model of the transducer transfer function,²³ \tilde{H}_{tr} , is inserted in the PA response integrand, Eq. (5). Integrating over the frequency range of the transducer results in the band-limited expansion:

$$V_{tr}(t) = \frac{\Gamma_a \mu_a E_0 \eta e^{-\mu_{eff} L}}{2} \int_{-f_0-(B_T/2)}^{f_0+(B_T/2)} \left(\frac{e^{-\alpha_s f L}}{\mu_a c_a + j\omega} \right) \times \tilde{H}_{tr}(f) e^{j\omega(t-(L/c_s))} df \quad (14)$$

where B_T and f_0 are the bandwidth and central frequency of the transducer, respectively. For the determination of the delay

time corresponding to the distance L (the peak value), we set $t = L/c_s$:

$$V_{tr} \left(t = \frac{L}{c_s} \right) = 2 \frac{\Gamma_a \mu_a E_0 \eta e^{-\mu_{eff} L}}{2} \times \left[\int_{f_0-(B_T/2)}^{f_0+(B_T/2)} \left(\frac{e^{-\alpha_s f L}}{\mu_a c_a + j\omega} \right) \tilde{H}_{tr}(f) df \right]_{real}. \quad (15)$$

The produced SNR can be calculated from the following definition:²⁷

$$SNR = \frac{\text{Maximum output peak power}}{\text{Output noise power}} = \frac{|s(t)|_{\max}^2}{N_{out}}. \quad (16)$$

Equations (15) and (16) give the TD-PA SNR at the peak of the pressure pulse:

$$SNR_{Puls} = \frac{(\Gamma_a \mu_a E_0 \eta e^{-\mu_{eff} L})^2 \left| \int_{f_0-(B_T/2)}^{f_0+(B_T/2)} \left(\frac{e^{-\alpha_s f L}}{\mu_a c_a + j\omega} \right) \tilde{H}_{tr}(f) df \right|_{real}^2}{N_0 B_T}, \quad (17)$$

where N_0 is the mean noise power of the detected signal. N_{out} in Eq. (16) is the total output noise power and includes thermal noise as well as other unfavorable signals.²⁸

B. Linear chirp FD-PA mode

In the FD method, the delay time is determined from the cross-correlation of output and input signals. The cross-correlation function can be calculated as

$$R(t) = \mathbf{F}^{-1} \{ \tilde{V}_{tr}(f) \cdot \tilde{I}_0^*(f) \}, \quad (18)$$

or from Eqs. (4) and (5),

$$R(t) = \mathbf{F}^{-1} \left\{ \frac{\Gamma_a e^{-\mu_{eff} L}}{2} \left(\frac{\mu_a}{\mu_a c_a + j\omega} \right) e^{-j(\omega/c_s)L} e^{-\alpha_s f L} \times \eta H_{tr}(f) \tilde{I}_0(f) \cdot \tilde{I}_{ref}^*(f) \right\}. \quad (19)$$

The input signal is the laser intensity $I_0(t)$ [W/cm²]. For a linear frequency modulation waveform,

$$I_0(t) = A_I \left[1 + \cos \left(\omega_c t + \frac{\pi B_{ch}}{T_{ch}} t^2 \right) \right], \quad -\frac{1}{2} T_{ch} \leq t \leq \frac{1}{2} T_{ch}, \quad (20)$$

where A_I is the average laser intensity, calculated by measuring the laser power and the beam spotsize; $\omega_c = 2\pi f_c$, where f_c is the center frequency of the chirp; T_{ch} and B_{ch} are the

duration and frequency sweep range of the chirp. In the cross-correlation process, the detected signal is multiplied by the complex conjugate of the input signal. The dc part of the input signal is eliminated and the amplitude of the waveform is normalized to produce the reference signal $\tilde{I}_{ref}^*(f)$. The peak value of the cross-correlation is the total spectral energy of the matched filter output:

$$R_{Max.} \left(t = \frac{L}{c_s} \right) = \frac{\Gamma_a e^{-\mu_{eff} L}}{2} \int_{-\infty}^{+\infty} \left(\frac{\mu_a}{\mu_a c_a + j2\pi f} \right) e^{-\alpha_s f L} \times \eta \tilde{H}_{tr}(f) \tilde{I}_0(f) \cdot \tilde{I}_{ref}^*(f) df. \quad (21)$$

For the frequency range of the chirp, we can substitute $\tilde{I}_0(f) \cdot \tilde{I}_{ref}^*(f) \approx A_I (T_{ch}/4B_{ch})$.²⁴ Combining the in-phase and the quadrature signals, we obtain

$$R_{Max.} \approx \Gamma_a \mu_a \eta e^{-\mu_{eff} L} \left(A_I \frac{T_{ch}}{4B_{ch}} \right) \times \left[\int_{f_c-(B_{ch}/2)}^{f_c+(B_{ch}/2)} \left(\frac{e^{-\alpha_s f L}}{\mu_a c_a + j\omega} \right) \tilde{H}_{tr}(f) df \right]_{Max.}, \quad (22)$$

where “Max.” refers to the maximum of real or imaginary parts. These two maxima do not occur at the same delay time; however, the quadrature maximum is also located inside the axial resolution limit (FWHM) of the envelope (amplitude) signal. Now, the output SNR of the matched filter can be calculated from Eq. (16) in a manner similar to the TD-PA:

$$\text{SNR}_{\text{CW}} = \frac{\left(\Gamma_a \mu_a e^{-\mu_{\text{eff}} L} \eta A_I \frac{T_{\text{ch}}}{4B_{\text{ch}}} \right)^2 \left| \int_{f_c - (B_{\text{ch}}/2)}^{f_c + (B_{\text{ch}}/2)} \left(\frac{e^{-\alpha_s f L}}{\mu_a c_a + j\omega} \right) \tilde{H}_{\text{tr}}(f) df \right|_{\text{Max.}}^2}{N_0 \int_{f_c - B_{\text{ch}}/2}^{f_c + B_{\text{ch}}/2} \left| \sqrt{\frac{T_{\text{ch}}}{4B_{\text{ch}}}} \right|^2 df} \quad (23)$$

Any noise components outside the chirp bandwidth are automatically eliminated through matched filtering. The result is

$$\text{SNR}_{\text{CW}} = \frac{(\Gamma_a \mu_a \eta e^{-\mu_{\text{eff}} L} A_I)^2 T_{\text{ch}} \left| \int_{f_c - (B_{\text{ch}}/2)}^{f_c + (B_{\text{ch}}/2)} \left(\frac{e^{-\alpha_s f L}}{\mu_a c_a + j\omega} \right) \tilde{H}_{\text{tr}}(f) df \right|_{\text{Max.}}^2}{4N_0 B_{\text{ch}}^2} \quad (24)$$

From this expression it can be seen that the SNR is proportional to the product of the chirp duration and the square of the laser intensity. Referring to American National Standards Institute safety standards for laser MPE on human skin²⁹ for exposure duration between 100 ns and 10 s, the MPE is defined as

$$\text{MPE}(t) = 1.1 C_A t^{1/4} \quad [\text{J cm}^{-2}] \quad 100 \text{ ns} \leq t \leq 10 \text{ s}, \quad (25)$$

where C_A is a constant depending on the laser wavelength; $C_A = 5$ for 1064 nm.²⁹ Setting $t = T_{\text{ch}}$ and choosing the laser power and exposure duration according to MPE, Eq. (24) yields

$$\text{SNR}_{\text{CW}} \propto A_I^2 T_{\text{ch}} = \frac{(1.1 C_A)^2}{T_{\text{ch}}^{1/2}} \quad (26)$$

with $A_I = \text{MPE}(T_{\text{ch}})$, which can also be expressed as

$$\text{SNR}_{\text{CW}} \propto A_I^2 T_{\text{ch}} \propto A_I^{2/3}. \quad (27)$$

These relations indicate that by decreasing the laser exposure duration and increasing the laser power corresponding to MPE regulations, the FD SNR will increase. Experimental results presented in Sec. IV B supports this conclusion.

C. SNR comparison between TD and FD PA with respect to MPE

We can estimate the detected signal and SNR in both modalities for our high frequency transducer using physical parameters of the tissue: $\Gamma_a = 0.24$, $c_a = 1500$ m/s, $\mu_{\text{eff}} = 1.5$ cm⁻¹, a typical depth and laser spotsize at the surface: $L = 2$ cm, $W = 4$ mm, MPE for pulsed laser $E_0 = 0.1$ J/cm², assuming an absorption coefficient $\mu_a = 2$ cm⁻¹. The laser fluence reaching the absorber can be estimated from Eq. (3) to be 5 J/m². For the pulsed irradiation mode, the peak pressure generated is 120 Pa, Eq. (11), and the voltage detected by the high frequency transducer is 248 μ V (Eq. (15)). To estimate the SNR, the noise level must be determined. The root-mean-square (rms) voltage due to thermal noise for a piezoelement operating in the open circuit mode is estimated from the Nyquist formula for a capacitor plate:^{13,30}

$$U_{\text{rms}} = \sqrt{\frac{4k_B T_0}{C_0}} = \frac{128}{\sqrt{C_0(\text{pF})}} \quad [\mu\text{V}] \quad (28)$$

where k_B is the Boltzmann constant, T_0 is the absolute ambient temperature, and C_0 is the electric capacitance of the transducer. The unclamped capacitance of the transducer was measured first; then utilizing the permittivity of the clamped and unclamped piezomaterial, the clamped capacitance was estimated.²⁵ It was found to be 462 pF for our high frequency transducer, with Eq. (28) yielding 6 μ V for the thermal noise level for this transducer. Thus, the system SNR is found to be 32.3 dB.

For the FD mode, assuming exposure duration of 0.8 ms, laser intensity of 6.5 W/cm², and frequency sweep from 200 kHz to 3 MHz (the choice of bandwidth is discussed in Refs. 23 and 31), the laser intensity impinging on the absorber surface was estimated (Eq. (3)) to be 325 W/m². From Eq. (22), the cross-correlation peak is found to be 0.0023 μ Vs. To compare the cross-correlation peak with the thermal noise level as shown in Eq. (23), the peak value must be divided by $\sqrt{T_{\text{ch}}/4B_{\text{ch}}} = 2.67 \times 10^{-4}$ s to take the account for the cross-correlation operation effect on the noise level. Thus, the normalized cross-correlation peak is found to be 8.6 μ V. The cross-correlation process eliminates any noise outside the chirp bandwidth. Since the utilized FD bandwidth was $\sim 40\%$ of the TD bandwidth; therefore, the noise level after cross-correlation was estimated to be 2.6 μ V. The theoretical FD-PA SNR is 10.4 dB which is 22 dB smaller than the pulsed mode.

The TD to the FD modality ratio of SNRs may be calculated using the foregoing signal theory. The transducer is normally considered to be the principal noise source.³⁰ Therefore, the average noise power (N_0) can be identical in both cases, and Eqs. (17) and (24) yield

$$\frac{\text{SNR}_{\text{Puls}}}{\text{SNR}_{\text{CW}}} = \frac{B_{\text{ch}} E_0^2 \left| \int_{f_0 - (B_T/2)}^{f_0 + (B_T/2)} \left(\frac{e^{-\alpha_s f L}}{\mu_a c_a + j\omega} \right) \tilde{H}_{\text{tr}}(f) df \right|_{\text{real}}^2}{B_T A_I^2 \frac{T_{\text{ch}}}{4B_{\text{ch}}} \left| \int_{f_c - (B_{\text{ch}}/2)}^{f_c + (B_{\text{ch}}/2)} \left(\frac{e^{-\alpha_s f L}}{\mu_a c_a + j\omega} \right) \tilde{H}_{\text{tr}}(f) df \right|_{\text{Max.}}^2} \quad (29)$$

If both methods use the same detection bandwidth, $B_{\text{ch}} = B_T$, the result is

$$\frac{\text{SNR}_{\text{Puls}}}{\text{SNR}_{\text{CW}}} \approx \frac{4E_0^2 B_{\text{ch}}}{A_I^2 T_{\text{ch}}} \quad (30)$$

By substituting the -6 dB bandwidth of the transducers for both methods, and using the aforementioned values for the laser power, the SNR difference for the 0.5 MHz and 3.5 MHz

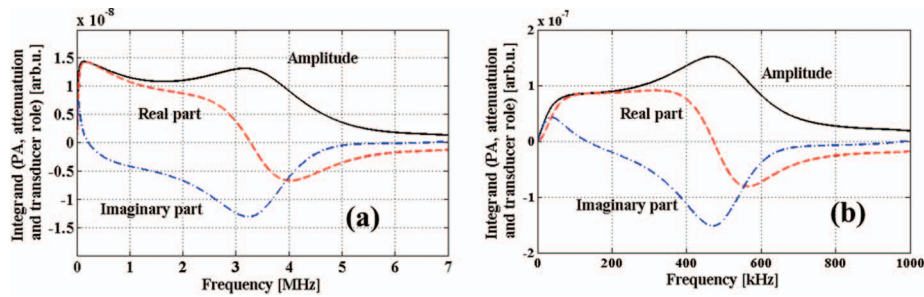


FIG. 5. (Color online) The system spectrum with combined PA, acoustic attenuation, and transducer effect (integrand in Eq. (32)) for (a) a high-frequency and (b) a low-frequency transducer (typical values of parameters used here: $\mu_a = 2 \text{ cm}^{-1}$, $c_s = 1.5 \text{ mm}/\mu\text{s}$, $L = 2 \text{ cm}$, $\alpha_s = 0.0863 \text{ Np/cm}$).

transducers will be 26 dB and 35 dB, respectively. These results are consistent with estimates by Maslov and Wang.¹⁵ However, our experiments exhibited much smaller differences in the SNR of the two modes. A more accurate estimate of the SNR difference must consider the limited bandwidth of the FD mode and the sources of noise in each modality. The optimal bandwidth for the FD mode can be less than half of the bandwidth used in pulsed detection.²³ Integrating across the limited bandwidth of the FD mode, compared with the wide bandwidth used in the pulsed detection, Eq. (29) gives

$$\begin{aligned} \frac{\text{SNR}_{Puls}}{\text{SNR}_{CW}} &= \frac{B_{ch} \left| \int_{B_T} \frac{e^{-\alpha_s f L}}{\mu_a c_a + j\omega} \tilde{H}_{tr}(f) df \right|_{\text{real}}^2}{B_T \left| \int_{B_{ch}} \frac{e^{-\alpha_s f L}}{\mu_a c_a + j\omega} \tilde{H}_{tr}(f) df \right|_{\text{Max.}}^2} \left(\frac{4E_0^2 B_{ch}}{A_I^2 T_{ch}} \right) \\ &\equiv C_I \frac{4E_0^2 B_{ch}}{A_I^2 T_{ch}}. \end{aligned} \quad (31)$$

The coefficient C_I is calculated using the complete transducer bandwidth for TD and optimal bandwidth for FD: 7.5 MHz vs. 0.2–3 MHz and 1 MHz vs. 200–800 kHz, for high and low frequency transducers, respectively. C_I is obviously a function of μ_a , α_s , and L . For an inclusion of 2 cm^{-1} absorption coefficient, located at 2 cm depth and the acoustic attenuation of human breast, C_I is 0.14 and 0.08 for high and low frequency transducers, respectively. Figures 5(a) and 5(b) show the integrand in Eq. (31) which determines C_I values. This composite spectrum represents the combination of the PA effect, acoustic attenuation, and transducer transfer function.

The foregoing SNR calculations are based on the ratio of signal peak to transducer thermal noise. However, there are other factors which deteriorate the SNR: sidelobes in the FD mode and baseline oscillations which appear in the pulsed transient response. Experiments in Sec. IV show that the baseline oscillation is the main TD-PA SNR limiting factor. These oscillations are generated by the direct incident of photons from the intense laser pulse on the transducer surface and are present in backward-scattered as well as forward PA arrangements.^{6,32} A major part of these fluctuations can be eliminated by high-pass filtering of the detected signal. These oscillations are also present in the FD-PA mode; however, the cross-correlation process collects them to zero delay time and thus eliminates them from the range of peak response. In addition, the inherently lower power of the FD-mode and the limited bandwidth of the chirp which acts as a bandpass fil-

ter automatically produce a smaller baseline. In the FD mode, signal sidelobes generated by the cross-correlation operation itself can be another cause of reduction in the SNR. Judicious selection of chirp bandwidth can take advantage of the transducer transfer function at low frequencies, coupled with the PA effect and acoustic attenuation at high frequencies to filter the signal and reduce the sidelobe level without extra windowing.³¹

The integrals in Eq. (31) can be modified by involving a high-pass filter in the TD-PA spectral energy and estimating a new ratio, C_{II} . Since the main source of noise, the baseline oscillations, is still not completely eliminated, the calculated SNR ratio should be considered as an upper limit:

$$\frac{\text{SNR}_{Puls}}{\text{SNR}_{CW}} \leq C_{II} \frac{4E_0^2 B_{ch}}{A_I^2 T_{ch}}. \quad (32)$$

By setting the low cut-off frequency at 150 and 100 kHz for the high and low frequency transducers, respectively, the corresponding C_{II} values are found to be 0.12 and 0.037. Table I shows how variation of the absorption coefficient in the $0.1\text{--}10 \text{ cm}^{-1}$ range changes the C_I and C_{II} and corresponding SNR differences between TD and FD PA for both high- and low-frequency transducers. This table shows that with a low-frequency transducer, the system performance is strongly associated with the physical properties of the sample, while at high frequencies, the deviation due to absorption coefficient variation is small.

IV. EXPERIMENTAL RESULTS

A. SNR and contrast comparison at low frequencies

A series of experiments were performed, intending to compare the SNR and contrast of FD and pulsed PA methods in the low frequency range, centered at 500 kHz. Two black rubber squares $4 \times 4 \text{ mm}^2$ and $2 \times 2 \text{ mm}^2$ were placed at a depth of 16 mm in 0.47% Intralipid solution. The effective optical attenuation of this solution resembles breast tissue at 1064 nm.²⁰ The pulsed laser energy was fixed at 100 mJ/cm^2 and 30 averages were employed at each position (additional averaging did not enhance the SNR). The intensity of the CW laser irradiating the sample was 6.5 W/cm^2 , and the total laser exposure time was 800 ms (800 one-ms chirps). The chirp frequency sweep was set between 200 and 800 kHz. Images were produced by raster-

TABLE I. The variation of SNR differences between TD and FD PA modalities versus the absorption coefficient for both employed transducers.

μ_a	High-frequency transducer				Low-frequency transducer			
	C_I	C_{II}	Estimated SNR difference before and after high-pass filtering (dB)		C_I	C_{II}	Estimated SNR difference before and after high-pass filtering (dB)	
0.1	0.1486	0.1136	24.4	23.2	0.0759	0.0093	14.8	5.6
0.2	0.1481	0.1139	24.4	23.2	0.0761	0.0105	14.8	6.2
0.5	0.1464	0.1149	24.3	23.3	0.0767	0.0144	14.8	7.5
0.7	0.1454	0.1156	24.3	23.3	0.0771	0.0172	14.8	8.3
1	0.1439	0.1164	24.2	23.3	0.0779	0.0215	14.9	9.3
2	0.1397	0.1187	24.1	23.4	0.0814	0.0366	15.1	11.6
4	0.1337	0.1213	23.9	23.5	0.0920	0.0648	15.6	14.1
6	0.1300	0.1223	23.8	23.5	0.1063	0.0899	16.2	15.5
10	0.1265	0.1232	23.7	23.6	0.1442	0.1397	17.5	17.4

scanning with 1-mm steps in both horizontal and vertical directions.

Figures 6(a) and 6(b) depict the fixed delay-time cross-section corresponding to the position of the squares in the Intralipid solutions, produced by FD-PA and TD-PA, respectively. The location of the inclusions is shown with the dashed squares in the picture. In both pictures, the large square can be identified; however, the small black rubber square is almost unrecognizable, more so in the TD mode than in the FD mode. In general, the images suffer from poor lateral resolution due to the low spatial resolution of the transducer which is 5.4 mm.³³ Nevertheless, the boundaries of the FD image are much better delineated than those of the TD image. The contrast factor (CF) is calculated by dividing the difference of mean signal in the absorber and background by mean signal in the background.^{34,31}

The dotted squares indicate the area outside the chromophore used as “background” in the CF calculations. CF values are indicated in the images.

Figures 6(c) and 6(d) show temporal (delay-time) cross-sectional slices of the large black rubber in Figs. 6(a) and 6(b), respectively. The corresponding signal traces in the

middle of the absorber for both imaging methods are depicted in Figs. 6(e) and 6(f). Higher contrast and SNR (calculated according to Eq. (16)) for FD-PA, are evident, even though the FD mode does not use the highest allowed power and corresponding duration with our set-up. The signal trace in Fig. 6(f) shows that the main reason for the poor contrast and SNR of the pulsed method is the deterministic baseline oscillations induced by radiation impinging on the transducer. To clarify this issue, in Fig. 7(a) the same signal trace as Fig. 6(f) is shown with two additional A-scans which were obtained away from the inclusion. This figure demonstrates the deterministic nature of the baseline (with a minor random component) which, therefore, cannot be eliminated by increasing the number of the averages, but various filtering methods may be used to reduce it.^{6,32} Figure 7(b) demonstrates the same transients after high-pass filtering with a cut-off frequency of 150 kHz. In the filtered signal trace the higher frequency oscillations are still detectable. A further increase of the filter cut-off frequency would also distort the bipolar form of the signal. The utilized high-pass filter reduced the maximum peak value, and, in addition to enhancing the SNR by ~ 10 dB, the second peak, the echo from the back of the absorber is also clearly

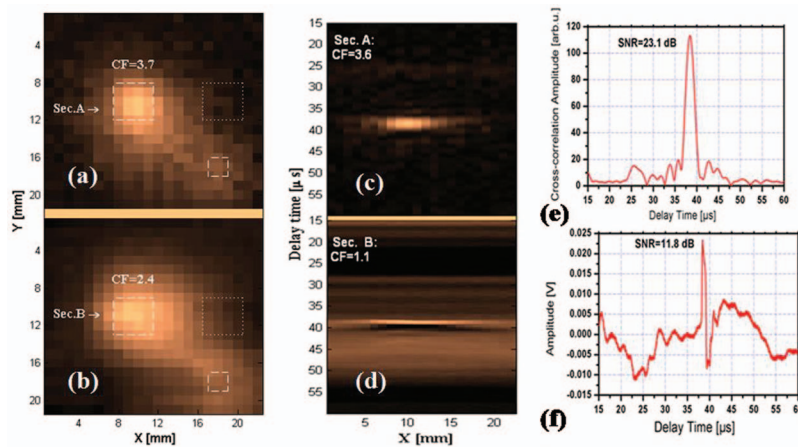


FIG. 6. (Color online) (a) FD-PA and (b) TD-PA fixed delay-time images utilizing a low frequency transducer. CW laser intensity was 6.5 W/cm^2 and exposure duration was 800 ms. Pulse fluence was 100 mJ/cm^2 . The positions of the inclusions are delineated with dashed lines. The dotted squares were used to calculate the CFs indicated in the images for the large black squares. (c) FD-PA and (d) TD-PA delay-time (depth cross-sectional) images. The corresponding section from (a) and (b) is indicated in the images. (e) and (f) A-scans corresponding to the center of the absorber in (c) and (d), respectively.

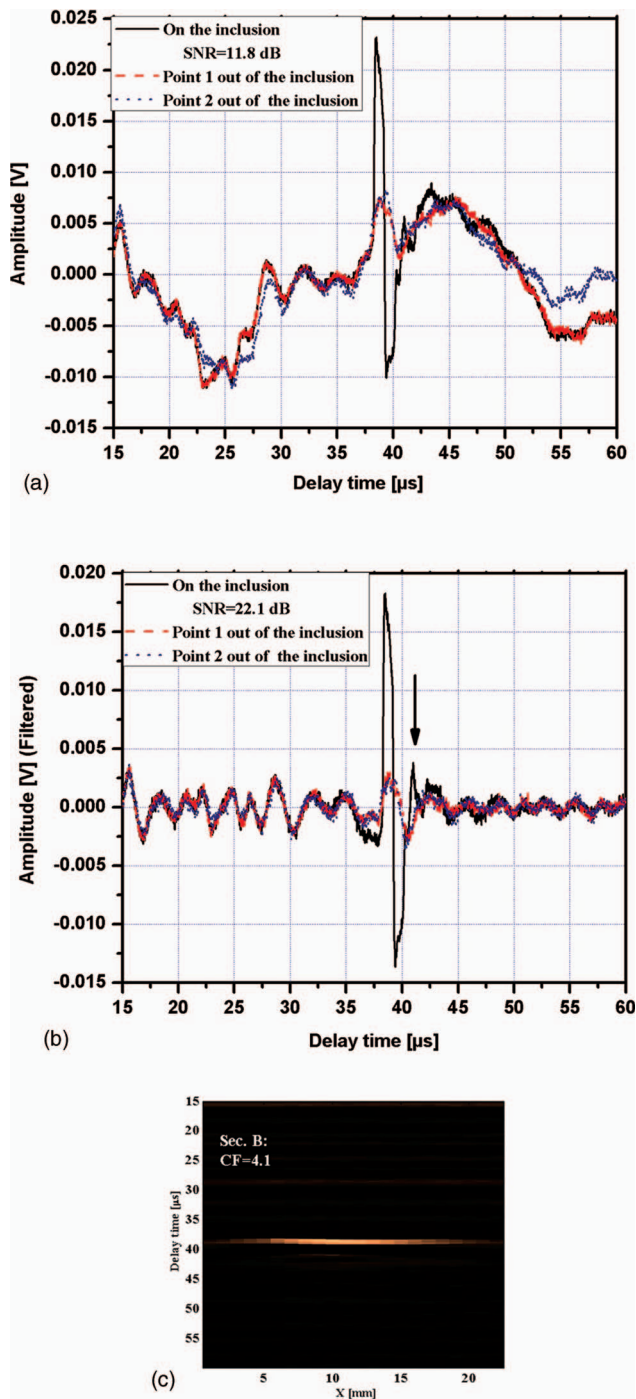


FIG. 7. (Color online) A-scans in three different locations; (a) before high-pass filtering, (b) after high-pass filtering, and (c) TD-PA depth-wise image after high-pass filtering.

recognizable (arrow). The inability to remove the baseline interference completely, especially when the baseline trace varies from location to location depending on the relative geometry of subsurface absorbers and scatterers, is a major factor in the pulsed PA SNR determination which is far more serious than the thermal (random) noise of the transducer. Figure 7(c) is the same image as Fig. 6(d), after high-pass filtering. It can be seen that the contrast of the pulsed delay-time cross-sectional image also increased proportionally. Filtering does not make any remarkable enhancement in the contrast of the fixed delay time image, Fig. 6(b). The SNRs of the

A-scans in the middle of the black rubber squares were 23.1 dB, 11.8 dB, and 22.1 dB for FD, pulsed, and high-pass filtered pulsed signals, respectively. As discussed earlier, the SNR difference between TD and FD PA is far less than the values derived by theory, with that of the FD mode actually being higher than the pulsed mode. The reason for this is that even after high-pass filtering the pulsed signal trace, the dominant source of the noise is the baseline fluctuation, which is not considered in the theoretical estimates. We also compared the axial resolution of both methods using the FWHM of the peak in each case. The FWHM of the FD-PA peak was $2.43 \mu\text{s}$, while that of the TD-PA was $0.86 \mu\text{s}$, and for the filtered pulsed signal trace, it was $0.82 \mu\text{s}$. However, these TD-PA values do not consider the complete length of the N-shaped acoustic profile (compression followed by rarefaction) which limits axial resolution (Sec. IV C).

B. SNR and contrast comparison at high frequencies

Upon increasing the laser power and reducing the exposure time within the safety limits, it is seen (Eqs. (26) and (27)) that the SNR of the FD-PA method can be increased. This was verified experimentally earlier²¹ and in this work with single point excitation of a subsurface absorber. The exposure time varied from 1 s to 250 ms and the laser power was varied from 5.5 W/cm^2 to 15.6 W/cm^2 , respectively, according to Eq. (26). An absorber ($\mu_a = 4 \text{ cm}^{-1}$) was embedded in 1 cm of highly concentrated Intralipid solution (0.47%). Figure 8(a) shows that the cross-correlation amplitude increases with increasing power and reduced exposure time. By increasing the power, the noise level also increased, but the increase is insignificant compared to the peak amplitude amplification. Figure 8(b) shows the SNR corresponding to this process. The experimental SNR changes were consistent with the theoretical prediction of Eq. (27) (Fig. 8(b), continuous line).

An experiment similar to that of Sec. IV A was performed next with a high-frequency transducer (3.5 MHz); the sample and Intralipid solution had the same parameters and configuration as those used with the low-frequency transducer. The absorber was located at the focal distance of the transducer ($\sim 2.5 \text{ cm}$). The lateral resolution of this transducer was 0.87 mm based on the manufacturer's data,³³ so scans were performed with 0.5 mm step-size. In this experiment, the pulsed laser fluence was fixed at the MPE level, 100 mJ/cm^2 . FD-PA images were produced with two combinations of laser power and exposure time; 6.5 W/cm^2 and 800 ms, and 15.6 W/cm^2 and 250 ms. These cases will henceforth be referred to as high-power and low-power FD-PA, respectively. For the high-power experiment, the bottoms of the black rubber squares were aligned, Fig. 9(c). The frequency sweep range was $200 \text{ kHz} - 3 \text{ MHz}$. Figures 9(a)–9(c) show fixed delay time images at the location of the absorbers. The dashed squares show the actual position of the samples. The dotted quadrangles show the area outside the chromophore used for contrast comparison. For the large black rubber, the CF was calculated by comparing the right half of the absorber area with the adjacent dotted quadrangle, and for the smaller absorber, the total area of the absorber was compared to the

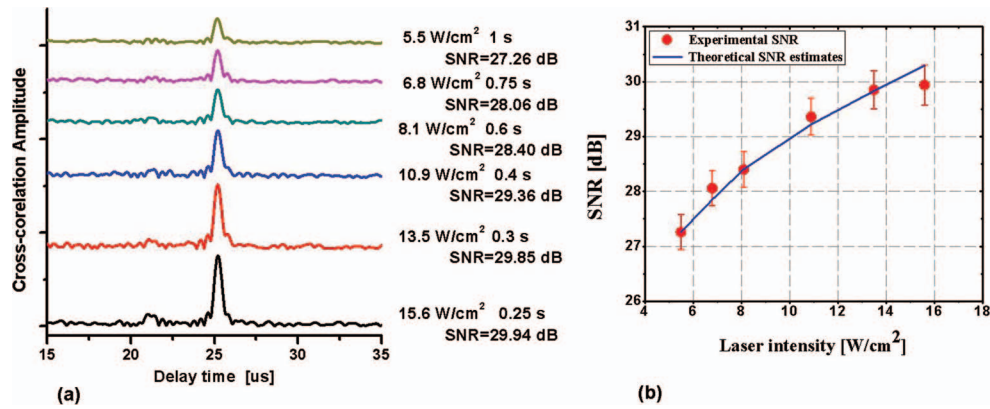


FIG. 8. (Color online) (a) FD-PA signal traces using a high frequency transducer: exposure duration decrease and laser power increase according to the safety standard from top to bottom. (b) SNR enhancement corresponding to laser power increase, exposure duration decrease. The theoretical SNR augmentation is calculated from Eq. (27).

adjacent dotted square. The images from top to bottom (Figs. 9(a)–9(c)) correspond to the low-power FD-PA, pulsed, and high-power FD-PA, respectively. It can be seen that the FD method provides better contrast. Furthermore, the high-power FD-PA images of both absorbers, Fig. 9(c), are well contained within the boundaries of the actual absorbers, thus exhibiting higher spatial resolution than the pulse PA counterparts. The delay-time (equivalently: depth-wise) cross-sectional images are depicted in Figs. 9(d)–9(i). The left column images are associated with the large black rubber square and the right

column images correspond to the small black rubber square. The order from top to bottom is similar to Figs. 9(a)–9(c).

The A-scan traces at the center of the square absorbers are shown in Fig. 10. The order of A-scans is similar to Figs. 9(d)–9(i). Once again, it can be seen that despite the simplified theoretical predictions of Sec. III C, the SNRs are very close: 23.2 vs. 26.1 dB and 20.5 vs. 24.8 dB for high-power FD-PA and TD-PA, respectively. This is due to the baseline oscillations in the pulsed transient, even after high-pass filtering which increased the SNR of TD-PA by 4 dB.

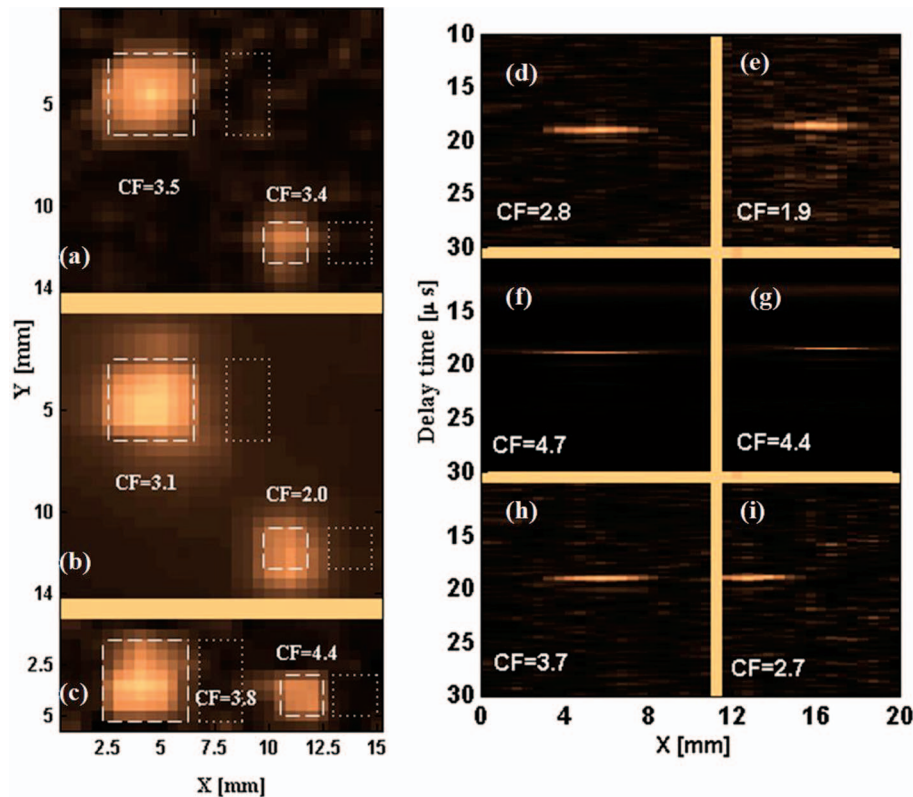


FIG. 9. (Color online) (a)–(c) Fixed delay-time images at a depth of 16 mm in 0.47% Intralipid solution (high frequency transducer): (a) generated with low-power FD-PA, (b) generated with TD-PA, and (c) generated with high-power FD-PA. The positions of the inclusions are delineated with dashed lines. The dotted quadrangles were used to calculate CFs indicated in the images for both black rubber squares. (d)–(i) Delay-time images: (d) and (e) low-power FD-PA image of large and small rubber squares, respectively. (f) and (g) high-pass filtered TD-PA image of large and small rubber squares, respectively. (h) and (i) high-power FD-PA image of large and small rubber squares, respectively.

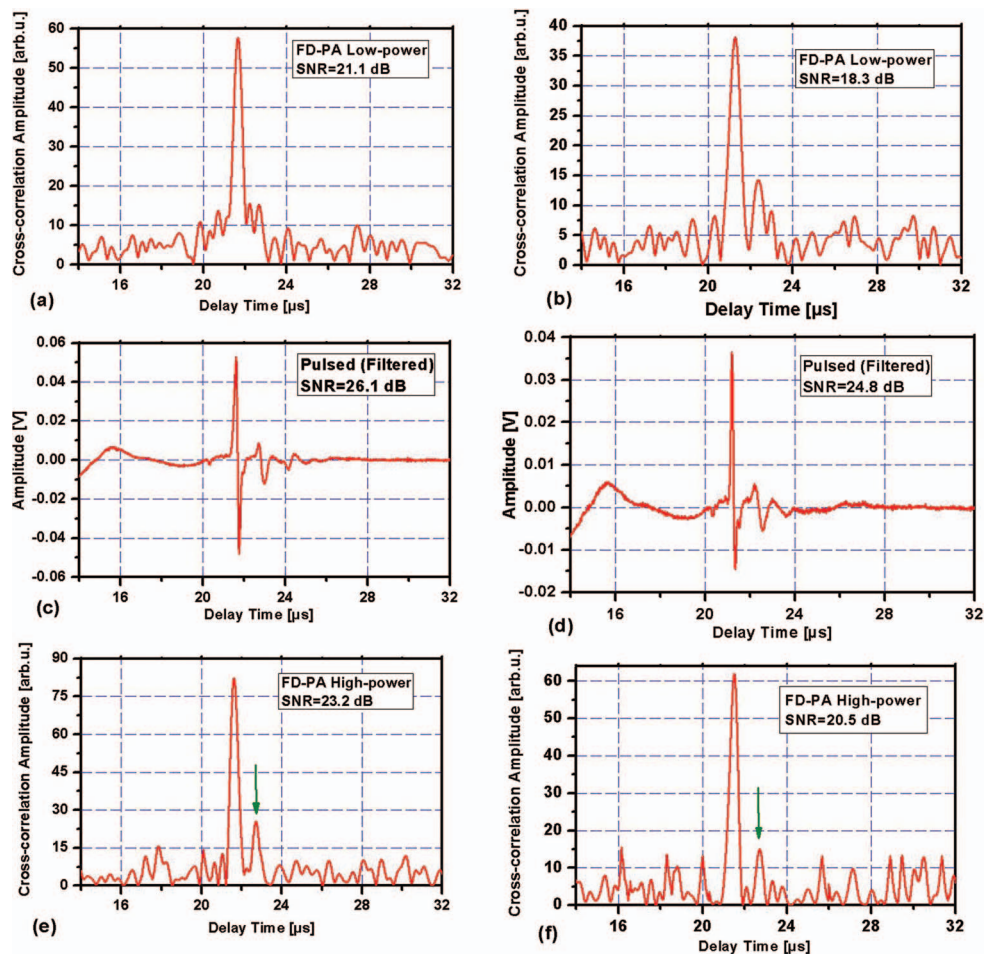


FIG. 10. (Color online) The A-scans at the center of the absorbers of Fig. 9, generated by low-power FD-PA from (a) large and (b) small rubber squares; TD-PA after high-pass filtering from (c) large and (d) small rubber squares; high-power FD-PA from (e) large and (f) small rubber squares.

The axial resolution (FWHM) of the FD signal peak was $0.46 \mu\text{s}$ (high-power case), while for the TD-PA peak, it was $0.164 \mu\text{s}$ (filtered signal). However, the presence of the rarefaction zone (N-shape) which follows the compression peak increases the effective FWHM of the TD-PA mode resulting in strongly compromised axial resolution as shown in Sec. IV C. Increasing the intensity in the FD method or filtering the TD signal had a negligible effect on axial resolution.

To show the image improvement effectiveness of the high-power, short-duration FD-PA method, an experiment was conducted with the same sample at a depth of 22 mm in 0.47% Intralipid solution. This depth was chosen, as it is the limit of FD-PA detection for this absorber with low laser intensity. Figures 11(a) and 11(b) show the cross-sectional images using the same power and exposure time combinations (6.5 W/cm^2 and 800 ms, and 15.6 W/cm^2 and 250 ms). The signal traces at the center of the black rubber squares are shown for both cases in Figs. 11(c)–11(d). The images clearly show the superior SNR of the top signal traces corresponding to the high-power, short-duration chirp case.

C. Maximum detectable depth and axial resolution

Another experiment investigated how deep a chromophore location could be detected with the TD and

FD-PA modalities, employing a high frequency transducer. The pulsed signals were filtered, and the pulsed laser fluence was set to the MPE limit of 100 mJ/cm^2 . The CW laser was also adjusted in terms of intensity and exposure time, 15.6 W/cm^2 and 250 ms, as per the MPE safety limit.²⁹ The chromophore was a piece of plastisol with an absorption coefficient of 4 cm^{-1} ,³⁵ located in 0.47% Intralipid solution. In Fig. 12, the SNR of FD-PA at various depths is compared with that of TD-PA, both before and after high-pass filtering. It can be seen that in the high frequency range, the pulsed method was able to detect a normal absorbing chromophore down to 22 mm below the surface and beyond. FD-PA with the described power and exposure time could only detect to a maximum depth of 18 mm. Experiment with the low-frequency transducer exhibits comparable depth detectivity of FD and TD PA as reported earlier by our group.²⁰

The axial resolution of both methods for a single absorber interface was compared in Secs. IV A and IV B, indicating an apparent superior resolution for TD-PA due to the wider bandwidth. An experiment was designed to test the capability of both methods to recognize two depth-wise adjacent absorbers within a very close distance, a form of Rayleigh axial resolution test. The sample was a layer of 1-mm thick plastisol strip separated from a thick plastisol piece by transparent layers of tape. The axial distance

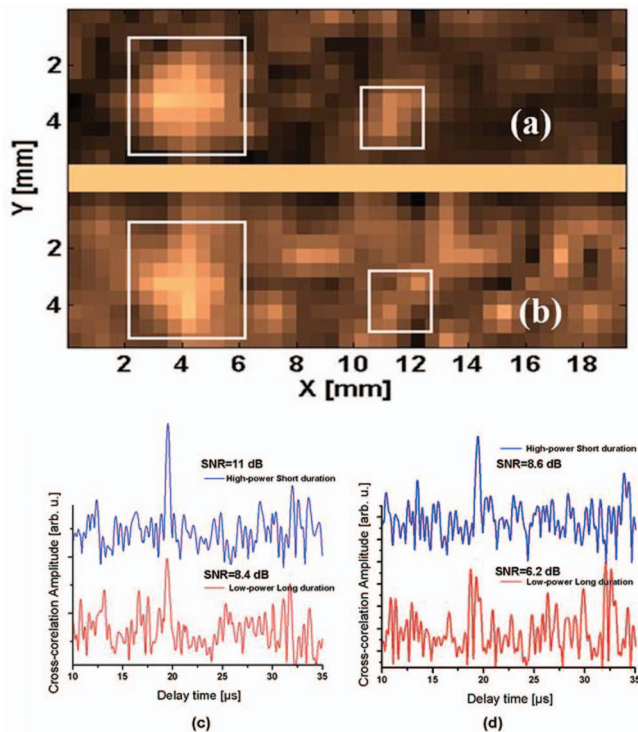


FIG. 11. (Color online) Fixed-delay image of the black rubber squares of Fig. 9 at the depth of 22 mm in Intralipid solution (0.47%): (a) High power, short duration; (b) low power, long duration FD-PA; (c) A-scans at the center of the large black rubber square employing high power (top) and low power (bottom) exposure.

between the two plastisol pieces was ~ 0.9 mm and the absorption coefficient of both samples was 9 cm^{-1} . The sample was placed at a depth of 1 cm in low-concentration Intralipid solution (0.05%). The TD-PA pulse fluence was 100 mJ/cm^2 and the CW laser intensity was 15.6 W/cm^2 with a frequency range of 200 kHz–3 MHz. The A-scans are compared in Figs. 13(a) and 13(b). The pulsed transient clearly exhibits high resolution of both absorbers, however, with strong, and possibly confusing, baseline perturbations, while the FD signal peaks from each absorber only partially over-

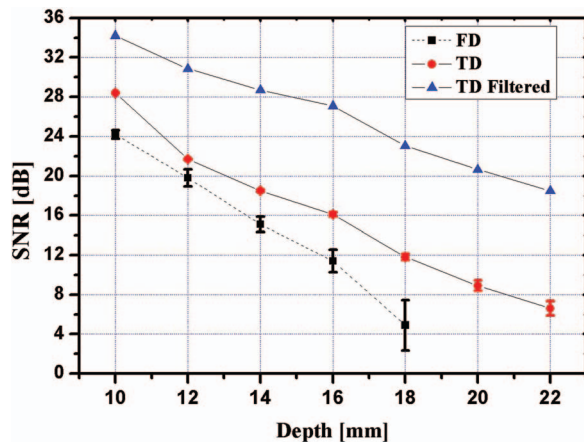


FIG. 12. (Color online) High-frequency transducer signal SNR at different depths, generated by the FD method and the pulsed method before and after high-pass filtering. The absorber is a plastisol with absorption coefficient of 4 cm^{-1} located in 0.47% Intralipid solution.

lapped. Figure 13(c) shows the signal trace corresponding to the inverse of the standard deviation of the phase (ISDP) and Fig. 13(d) is a combination (multiplication) of Fig. 13(c) with the amplitude signal.³¹ The combination trace has the distinct advantages of improved FWHM and greatly suppressed baseline. The effective axial resolution (FWHM) of the peaks is shown in each of the traces of Fig. 13. The complete images of the sample generated by TD-PA, FD-PA, and combined amplitude and ISDP are depicted in Figs. 14(a)–14(c). Figures 13(c) and 14(c) demonstrate superior FD-PA axial resolution, peak separation, and contrast over their TD-PA counterparts.

In principle, additional increase in the axial resolution of the FD-PA mode can be affected through frequency bandwidth increase. The foregoing experiment was repeated with the FD method using the frequency range of 200 kHz–5 MHz; however, only minor improvement in the axial resolution was observed.²⁴ This is due to the fact that the combined low-pass effects of PA and acoustic attenuation make any expansion in high-frequency range less effective. Adversely, increasing the bandwidth from the optimal condition decreases the SNR thereby rendering any attempts for improvement in axial resolution ineffective.

V. DISCUSSION

Using a comprehensive theoretical model including the various fundamental elements and processes involved in PA imaging, the signal and SNR for both pulsed and FD modes were estimated. It was further shown that the associated experimental results exhibit much smaller SNR differences than the theory implies. Experiments with a black rubber square at 16 mm depth of tissue-simulating Intralipid solution employing a high-frequency transducer resulted in ~ 4 dB higher SNR for the pulsed mode after high-pass filtering. A similar experiment with a low-frequency transducer exhibited fully comparable SNRs. Therefore, a more comprehensive investigation of all noise sources as well as baseline oscillations was undertaken to improve the estimates. Using inequality (32), along with increasing laser power and decreasing chirp duration, the crossing-point where the SNR difference between the TD and FD modalities approaches zero can be determined. The maximum allowable laser intensity (A_I) depends on the exposure time (T_{ch}) with SNR given by Eq. (26). Substituting A_I and T_{ch} in inequality (32), the maximum SNR difference between the two methods can be estimated and the results for both transducers are plotted in Fig. 15. The crossing-point for the low frequency transducer is ~ 5 ms and for the high frequency transducer is $\sim 20 \mu\text{s}$. These exposure durations correspond to 290 W/cm^2 and 3270 W/cm^2 , respectively. Employing shorter exposure times and correspondingly higher laser intensity, the PA system can deliver FD signals with SNR higher than the pulsed mode. This is particularly encouraging for use with low-frequency US transduction designed for deep-seated tumor imaging, such as in breast cancer cases, as chirps of duration < 5 ms are readily attainable. Inequality (32) indicates an upper limit and experimental results have shown, in practice, that the crossing-points occur with much smaller intensities.

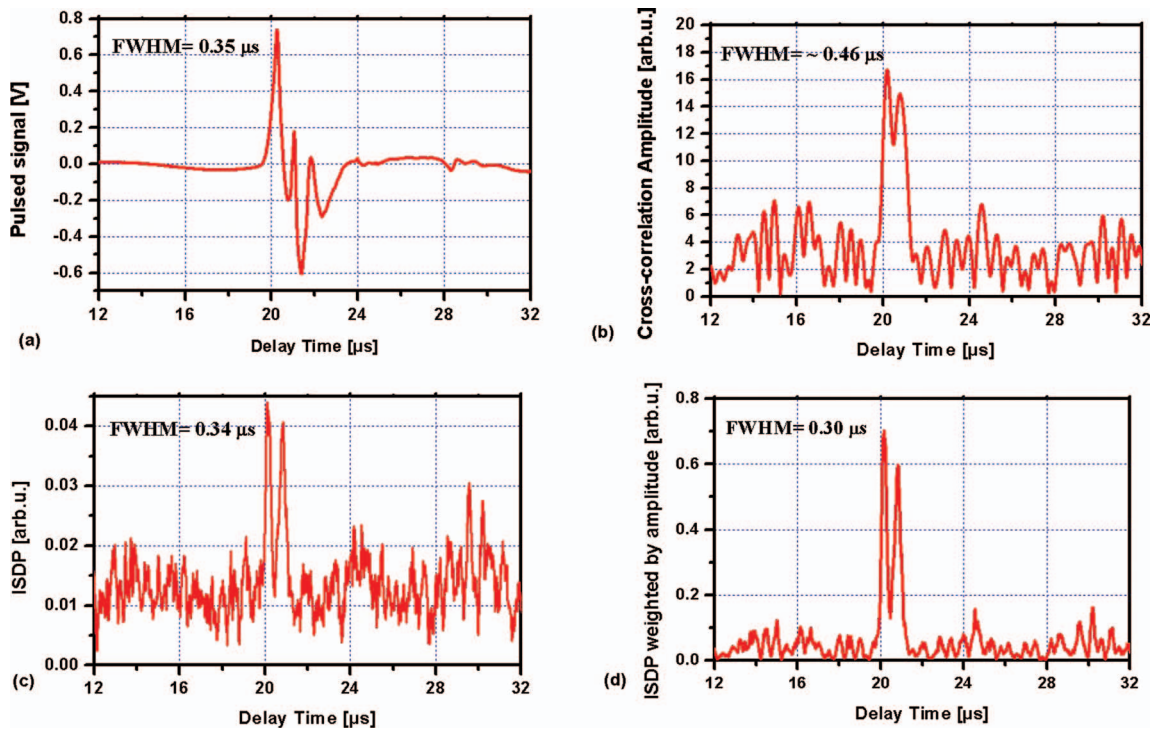


FIG. 13. (Color online) Axial resolution comparison: (a) TD-PA, (b) the FD-PA cross-correlation amplitude, (c) the FD-PA ISDP (derived from the phase signal), (d) FD-PA: combining amplitude and ISDP channels.

Regarding the high-frequency transducer, there are a few technical issues on utilizing very short chirp durations ($<20 \mu s$) and high laser intensities for the FD mode: The short chirp duration reduces the frequency resolution of the modulating waveform. Even though cross-correlation processing eliminates the oscillating interfering baseline by collecting its energy to a strong peak at zero delay-time, increasing the laser intensity will extend the peak's sidelobes which may overlap the earliest delay time range of interest. Prolonged signal averaging to improve SNR is limited by MPE constrains, by which the average intensity of long laser exposure is capped at

1 W/cm^2 ($\lambda = 1064 \text{ nm}$). Therefore, the maximum repetition frequency is 15.3 Hz for a $20 \mu s$ chirp. In other words, a laser intensity of 3270 W/cm^2 over $20 \mu s$ can be applied only every 65.4 ms . Similarly for the low-frequency transducer, a laser intensity of 290 W/cm^2 over 5 ms can be applied only every 1.45 s , which translates to a repetition frequency of 0.69 Hz .

The presented SNR formalism predicts that the TD versus FD SNR difference is smaller for low-frequency transducers, since SNR difference is proportional to chirp bandwidth (inequality (32)). Experimental results in Sec. IV exhibited approximately equal SNRs for the low-frequency transducer,

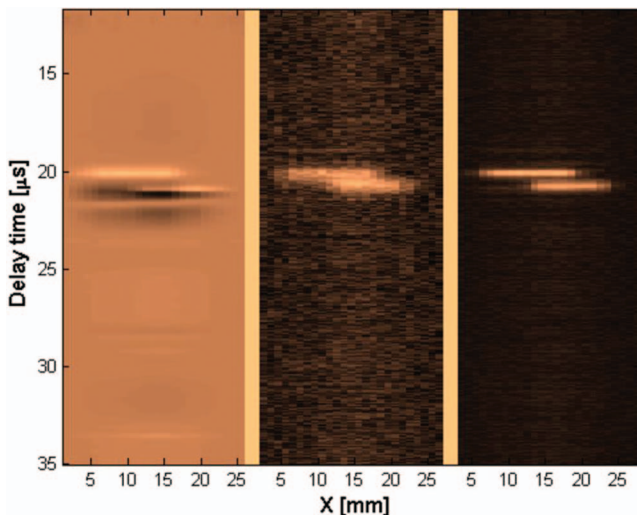


FIG. 14. (Color online) Images generated by (a) TD-PA, (b) FD-PA amplitude, (c) FD-PA amplitude filtered by ISDP signal.

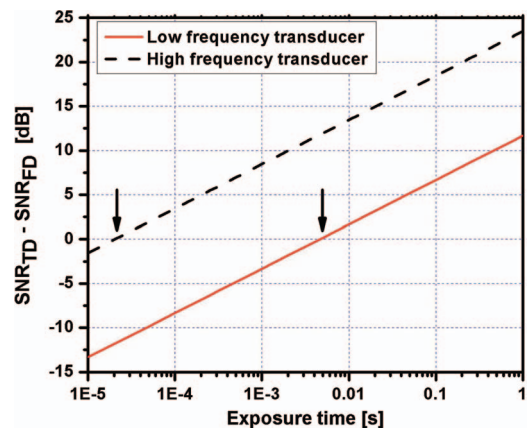


FIG. 15. (Color online) The predicted maximum SNR difference from inequality (32), between pulsed and FD-PA for the two types of transducers (0.5 and 3.5 MHz) used in our experiments. The arrows indicate the FD chirp lengths at which the SNR equals that of pulsed PA. In both cases the laser intensity (FD) and fluence (TD) are at the limit defined by the MPE. (See Ref. 29).

as opposed to ~ 6 dB for the high-frequency transducer. These results are also consistent with, and can justify, the previously reported experiments from our group.²⁰

Unlike PA imaging, the permissible intensity ratio between TD and FD ultrasonic imaging is ~ 440 according to guidelines for adult cardiac imaging.¹⁸ This intensity ratio can be compensated for by means of the large time-bandwidth product of FD and can even generate higher SNR for the FD US modality. In PA, however, the ratio of the permissible intensity for TD and FD modalities is six to seven orders of magnitude larger. While in ultrasound the transient pressure response is proportional to the square root of the ultrasound intensity, in PA, due to the energy conversion process, the generated transient is linearly proportional to the laser intensity. Therefore, to compensate for this large intensity difference, the time-bandwidth product of FD-PA should be 10^{12} – 10^{14} . This clarifies the more modest performance of FD-PA when compared with that of FD-US. However, in this work we have shown that by employing pulses of very short duration chirps, one can maximize the advantages of both methods and end up with higher SNR, contrast, and resolution using FD-PA.

The experimental results demonstrate that the contrast of the pulsed mode deteriorates due to baseline oscillations, while the contrast of the FD mode suffers from the weaker signal especially at the edges of absorbers. High-pass filtering the pulsed signal improves the delay-time (depth-wise) contrast, while employing high power, short chirps enhances the contrast of the FD method in both depth-wise and fixed delay time images.

The axial resolution of the pulsed PA transient not only depends on the frequency bandwidth, but is also a function of the physical properties of the absorber.³⁶ The axial resolution of FD-PA depends on chirp bandwidth which is narrower than that of pulsed PA. In addition, combining the in-phase and quadrature signals to generate the envelope amplitude reduces the axial resolution. The possibility of improving axial resolution for FD-PA by manipulating the bandwidth was examined. Our experiments demonstrated that increasing the frequency bandwidth drastically reduces the SNR which makes the method ineffective. However, combining the amplitude and ISDP signals increases the axial resolution of the FD method without adversely affecting the SNR. This is so because the phase signal has the axial resolution of the in-phase signal and the FWHM of both is narrower than that of the envelope cross-correlation amplitude. These facts offset the TD-PA bandwidth advantage to a considerable extent.

Additionally, the bipolar shape of the pulsed PA response introduces a large perturbation which reduces the probability of detecting two depth-wise adjacent chromophores. Therefore, the practical axial resolution of TD-PA is not defined by the FWHM of the peak alone, but by the baseline contrast in the presence of the negative (rarefaction) peak. As a result, the two-adjacent-absorber separation resolution of the FD mode (axial Rayleigh criterion) is superior to pulsed PA detection.

In conclusion, the cross-correlation PA modality (the PA Radar) has been shown to be very competitive with the conventional pulsed laser PA method in terms of all key imaging parameters: SNR, spatial and axial resolution, and contrast.

ACKNOWLEDGMENTS

The authors gratefully acknowledge the support of the Canada Foundation for Innovation (CFI), the Ontario Research Fund (ORF), and the Canada Research Chairs (CRC). They further acknowledge NSERC Strategic and Discovery Grants and the MRI Ontario Premier's 2007 Discovery Award in Science and Engineering to A.M.

- ¹M. Xu and L. V. Wang, *Rev. Sci. Instrum.* **77**, 041101 (2006).
- ²H. Li and L. V. Wang, *Phys. Med. Biol.* **54**, R59 (2009).
- ³A. A. Oraevsky, A. A. Karabutov, V. G. Andreev, and R. O. Esenaliev, *Proc. SPIE* **3597**, 352 (1999).
- ⁴V. G. Andreev, A. A. Karabutov, S. V. Solomatina, E. V. Savateeva, V. L. Aleynikov, Y. V. Zhulinc, R. D. Fleming, and A. A. Oraevsky, *Proc. SPIE* **3916**, 36 (2000).
- ⁵S. Manohar, A. Kharine, J. C. G. van Hespren, W. Steenbergen, and T. G. van Leeuwen, *Phys. Med. Biol.* **50**, 2543 (2005).
- ⁶S. A. Ermilov, T. Khamapirad, A. Conjusteau, M. H. Leonard, R. Lacewell, K. Mehta, T. Miller, and A. Oraevsky, *J. Biomed. Opt.* **14**(2), 024007 (2009).
- ⁷S. Manohar, S. E. Vaartjes, J. C. G. van Hespren, J. M. Klaase, F. M. van den Engh, W. Steenbergen, and T. G. van Leeuwen, *Opt. Express* **15**, 12277 (2007).
- ⁸Y. Fan, A. Mandelis, G. M. Spirou, I. A. Vitkin, and W. M. Whelan, *Proc. SPIE* **5320**, 113 (2004).
- ⁹Y. Fan, A. Mandelis, G. M. Spirou, I. A. Vitkin, and W. M. Whelan, *Phys. Rev. E* **72**, 051908 (2005).
- ¹⁰S. A. Telenkov and A. Mandelis, *J. Biomed. Opt.* **11**(4), 044006 (2006).
- ¹¹C. E. Cook and M. Bernfeld, *Radar Signals, An Introduction to Theory and Application* (Artech House, Norwood, MA, 1993).
- ¹²S. A. Telenkov, A. Mandelis, B. Lashkari, and M. Forcht, *J. Appl. Phys.* **105**, 102029 (2009).
- ¹³A. A. Oraevsky and A. A. Karabutov, *Proc. SPIE* **3916**, 228 (2000).
- ¹⁴G. Ku and L. V. Wang, *Opt. Lett.* **30**, 507 (2005).
- ¹⁵K. Maslov and L. V. Wang, *J. Biomed. Opt.* **13**(2), 024006 (2008).
- ¹⁶M. A. Choma, M. V. Sarunic, C. Yang, and J. A. Izatt, *Opt. Express* **11**, 2183 (2003).
- ¹⁷W. Edward, S. Teper, A. K. Nowinska, M. Milka, and D. Dobrowolski, *J. Cataract Refractive Surg.* **35**(8), 1410 (2009).
- ¹⁸M. O'Donnell, *IEEE Trans. Ultrason. Ferroelectr. Freq. Control* **39**, 341 (1992).
- ¹⁹M. H. Pedersen, T. X. Misaridis, and J. A. Jensen, *Proc.-IEEE Ultrason. Symp.* **2**, 1673 (2002).
- ²⁰S. A. Telenkov and A. Mandelis, *J. Biomed. Opt.* **14**(4), 044025 (2009).
- ²¹S. Telenkov and A. Mandelis, *Rev. Sci. Instrum.* **81**, 124901 (2010).
- ²²A. Petschke and P. J. La Rivière, *Biomed. Opt. Express* **1**(4), 1188 (2010).
- ²³B. Lashkari and A. Mandelis, *J. Acoust. Soc. Am.* **130**(2), 1313 (2011).
- ²⁴B. Lashkari, "Photoacoustic Imaging Using Chirp Technique: Comparison with Pulsed Laser Photoacoustics," Ph.D. dissertation, Mechanical and Industrial Engineering, University of Toronto, 2011.
- ²⁵R. S. C. Cobbold, *Foundations of Biomedical Ultrasound* (Oxford University Press, New York, 2007).
- ²⁶D. Leedom, G. Matthaie, and R. Krimholtz, *Electron. Lett.* **6**, 398 (1970).
- ²⁷M. Skolnik, *Introduction to Radar Systems* (McGraw-Hill, New York, 1962).
- ²⁸N. A. H. K. Rao, *Med. Biol. Eng. Comput.* **32**(2), 181 (1994).
- ²⁹American National Standards Institute, American National Standard for the Safe Use of Lasers: Standard Z136.1–2007, New York, 2007.
- ³⁰V. G. Andreev, A. A. Oraevsky, and A. A. Karabutov, *Proc.-IEEE Ultrason. Symp.* **2**, 1205 (2000).
- ³¹B. Lashkari and A. Mandelis, *Opt. Lett.* **35**(10), 1623 (2010).
- ³²R. O. Esenaliev, A. A. Karabutov, and A. A. Oraevsky, *IEEE J. Sel. Top. Quantum Electron.* **5**(4), 981 (1999).
- ³³"Panametrics-NDT: Ultrasonic Transducers," Olympus NDT, Catalogue 920-041C-EN, 2008.
- ³⁴M. S. Patterson and F. S. Foster, *Ultrason. Imaging* **5**, 195 (1983).
- ³⁵G. M. Spirou, A. A. Oraevsky, A. Vitkin, and W. M. Whelan, *Phys. Med. Biol.* **50**, N141 (2005).
- ³⁶A. A. Karabutov, N. B. Podymova, and V. S. Letokhov, *Appl. Phys. B* **63**(6), 545 (1996).